

PUBLISHED VERSION

Stanev, Todor; Engel, Ralph; Mücke, Anita G.; Protheroe, Raymond John; Rachen, Joerg P.

[Propagation of ultrahigh energy protons in the nearby universe](#) Physical Review D, 2000; 62(9):093005

© 2000 American Physical Society

<http://link.aps.org/doi/10.1103/PhysRevD.62.093005>

PERMISSIONS

<http://publish.aps.org/authors/transfer-of-copyright-agreement>

“The author(s), and in the case of a Work Made For Hire, as defined in the U.S. Copyright Act, 17 U.S.C.

§101, the employer named [below], shall have the following rights (the “Author Rights”):

[...]

3. The right to use all or part of the Article, including the APS-prepared version without revision or modification, on the author(s)' web home page or employer's website and to make copies of all or part of the Article, including the APS-prepared version without revision or modification, for the author(s)' and/or the employer's use for educational or research purposes.”

3rd April 2013

<http://hdl.handle.net/2440/12757>

Propagation of ultra-high energy protons in the nearby universe

Todor Stanev¹, Ralph Engel¹, Anita Mücke^{2,3}, Raymond J. Protheroe² & Jörg P. Rachen⁴

¹*Bartol Research Institute, University of Delaware, Newark, DE 19716, USA*

²*Dept. of Physics & Math Physics, University of Adelaide, SA 5005, Australia*

³*Université de Montréal, Département de Physique, Montréal, H3C3J7, Canada*

⁴*Sterrenkundig Instituut, Universiteit Utrecht, 3584 CC Utrecht, The Netherlands*

(Submitted to Phys. Rev. D: 31 March 2000; accepted 21 July 2000)

We present a new calculation of the propagation of protons with energies above 10^{19} eV over distances of up to several hundred Mpc. The calculation is based on a Monte Carlo approach using the event generator SOPHIA for the simulation of hadronic nucleon-photon interactions and a realistic integration of the particle trajectories in a random extragalactic magnetic field. Accounting for the proton scattering in the magnetic field affects noticeably the nucleon energy as a function of the distance to their source and allows us to give realistic predictions on arrival energy, time delay, and arrival angle distributions and correlations as well as secondary particle production spectra.

98.70.Sa, 13.85Tp, 98.62En, 98.70-f

I. INTRODUCTION

The world statistics of ultra high energy cosmic ray (UHECR) events of energy above 10^{20} eV has now grown to 20 events [1,2]. It is very difficult to accelerate particles to such high energies in astrophysical shocks, the process thought to be responsible for the majority of the galactic cosmic rays [3]. This has led to a large number of production models, many of them based on exotic particle physics scenarios [4]. The gyroradii of 10^{20} eV protons are significantly larger than our own Galaxy and this suggests an extragalactic origin [5] for any astrophysical scenario ($r_g = 100\text{kpc} \times (E/10^{20}\text{eV}) \times (1\mu\text{G}/B)$ with E and B being the proton energy and the magnetic field strength, respectively). The large distances between potential UHECR sources and Earth leads to another set of problems first pointed out independently by Greisen and by Zatsepin & Kuzmin, now widely known as the GZK effect [6]. UHECR protons interact with photons of the microwave background radiation and lose their energy relatively rapidly during propagation over distances of tens of megaparsecs. This should result in a cutoff in the cosmic ray spectrum at an energy just below 10^{20} eV.

Many different calculations [7–13], performed using various techniques, of the modification of the cosmic ray spectrum due to propagation have been published since the original suggestion. As a result, the general features of the cosmic ray spectrum after propagation are well established. Differences between the various approaches are, however, significant and the accuracy achieved is not sufficient for the interpretation of the existing experimental data, and more accurate calculations are needed for the expected significant increase of the experimental statistics [14–17].

Previous calculations can be divided into two classes dealing mainly with: (a) the energy loss processes [7–13], and (b) the deflection and scattering of protons in the extragalactic magnetic field [19,20,24]. The first group of calculations shows that small differences in the realization of the proton energy loss processes generate observable differences in the

predicted spectra at Earth. Such calculations, however, cannot establish an accurate relation between the distance of a potential source and the modification of the proton spectrum emitted by this source because the influence of the extragalactic magnetic field is neglected. Among the calculations of the second kind, Refs. [18–20] do not consider the proton energy losses in a satisfactory way, and Refs. [21–23] mostly discuss their results in a specific context. Only Achterberg *et al.* [24,25] give a detailed discussion of the fundamental aspects of UHECR propagation in extragalactic magnetic fields, which we are interested in here.

We present here calculations performed with the photoproduction event generator SOPHIA [26], which is proven to reproduce well the cross section and final state composition in nucleon-photon interactions for energies from the particle production threshold up to hundreds of GeV in the center-of-mass system. We also account for all other energy loss processes of UHECR nucleons, and calculate the proton deflection in the extragalactic magnetic field in three dimensions.

We restrict ourselves to proton injection energies up to 10^{22} eV, and consider (with few exceptions) proton propagation for source distances less than 200 Mpc. The calculations are carried out using a Monte Carlo technique, and we propagate individual protons injected as either a mono-energetic beam, or with energies sampled from a fixed source energy spectrum. This approach has the advantage of representing fluctuations in the proton energy losses very well, thereby giving us a good handle on the correlations between energy loss, time of flight and angular deviation of the flight direction. As we will show, these important UHECR characteristics are deeply interconnected. For a given source distance, there is a strong correlation between the amount of energy lost, the time delay, and the scattering angle.

Our calculations are thus mainly relevant to scenarios of UHECR acceleration at astrophysical shocks, for which 10^{22} eV is a very generous upper energy limit. With this paper we wish to establish limits for the distance of potential UHECR proton sources as a function of proton energy and the average

strength of the extragalactic magnetic field. We also study the angular distribution of UHECR with respect to the source direction (arrival angle) and the time delays after propagation over different distances. In addition, the neutrino fluxes produced during the propagation are presented.

The article is organized as follows. We describe the propagation method, including the relevant features of the event generator SOPHIA, in Section 2. Section 3 gives some interesting results on the propagation of mono-energetic proton beams, and compares our results with other work. Section 4 analyzes the formation and development of the primary and secondary particle spectra for protons injected with a power law spectrum. In section 5 we discuss the results, present our conclusions, and make suggestions for future work.

II. COSMIC RAY PROPAGATION

This section provides a description of our simulation code for propagating protons in intergalactic space. We treat energy losses due to hadronic and electromagnetic interactions of the nucleons with photons of the cosmic microwave background radiation as well as the deflection of particles by the intergalactic magnetic field. Although we present here only results on nucleon propagation in random magnetic fields, our approach also allows us to follow the particles in complicated magnetic field topologies. Because of the time-consuming detailed simulation of each nucleon propagation path by Monte Carlo, the propagation method described below is not suitable for calculations involving large cosmological distances.

A. Interactions and energy loss processes

Particles of energy $E > 10^{18}$ eV interact with photons of the cosmic microwave background radiation giving rise to secondary particle production and nucleon energy loss. The most important processes are:

- photoproduction of hadrons, and
- Bethe-Heitler (BH) production of e^+e^- pairs by protons.

We also account for the adiabatic losses due to cosmological expansion of the Universe, and for the decay of neutrons produced in hadronic production process. Since we restrict our calculation to models of UHECR acceleration in astrophysical shocks, and energies below 10^{22} eV, we consider only interactions with cosmic microwave background photons. The calculation of nucleon propagation at higher energies would require the use of models of the radio background (see e.g. Ref. [27]). Since we are not presenting results on the development of electromagnetic cascades initiated by secondary particles produced in proton-photon interactions, we can safely neglect interactions on the universal optical/infrared background as well. We keep track, however, of the individual energies of all secondaries of photoproduction interactions and are thus

able to show the spectra of neutrinos generated by primary protons after propagation over different distances.

Hadron production and energy loss in nucleon-photon interactions is simulated with the event generator SOPHIA [26]. This event generator samples collisions of nucleons with photons from isotropic thermal or power law energy distributions, using standard Monte Carlo techniques. In this paper the code has been used with a blackbody spectrum with $T = 2.726$ K to represent the cosmic microwave background. According to the respective partial cross sections, which have been parametrized using all available accelerator data, it invokes an interaction either via baryon resonance excitation, one-particle t -channel exchange (direct one-particle production), diffractive particle production and (non-diffractive) multiparticle production using string fragmentation. The distribution and momenta of the final state particles are calculated from their branching ratios and interaction kinematics in the center-of-mass frame, and the particle energies and angles in the lab. frame are calculated by Lorentz transformations. The decay of all unstable particles except for neutrons is treated subsequently using standard Monte Carlo methods of particle decay according to the available phase space. The neutron decay is implemented separately into the present propagation code. The SOPHIA event generator has been tested and shown to be in good agreement with available accelerator data. A detailed description of the code including the sampling methods, the interaction physics used, and the performed tests can be found in Ref. [26].

The Monte Carlo treatment of photoproduction is very important, because nucleons lose a large fraction of their energy in each interaction. As early as 1985 Hill & Schramm [7] pointed out that the use of a continuous energy loss approximation for this process neglects the intrinsic spread of arrival energies due to the variation of the energy loss ΔE per interaction, and the Poissonian distribution in the number of pion production interactions during propagation. This results in a certain “survival probability” of cosmic rays arriving at Earth with energies *above* the GZK-cutoff, as estimated in the assumption of continuous energy loss.

Fig. 1a shows the energy dependence of all parameters relevant to the average proton energy loss in the microwave background ($T=2.726$ K) for redshift $z = 0$. The photoproduction interaction length λ_{ph} for protons is shown as a dashed line. Denoting the proton-photon center-of-mass energy by \sqrt{s} , the interaction length can be written as [12]

$$\frac{1}{\lambda_{\text{ph}}(E)} = \frac{1}{8E^2\beta} \int_{\epsilon_{\text{th}}}^{\infty} d\epsilon \frac{n(\epsilon)}{\epsilon^2} \int_{s_{\text{min}}}^{s_{\text{max}}(\epsilon, E)} ds (s - m_p^2 c^4) \sigma_{p\gamma}(s) \quad (1)$$

with

$$s_{\text{min}} = (m_p c^2 + m_{\pi^0} c^2)^2 \quad (2)$$

$$s_{\text{max}}(\epsilon, E) = m_p^2 c^4 + 2E\epsilon(1 + \beta) \quad (3)$$

$$\epsilon_{\text{th}} = \frac{s_{\text{min}} - m_p^2 c^4}{2E(1 + \beta)}, \quad \beta^2 = 1 - \frac{m_p^2 c^4}{E^2}. \quad (4)$$

Here E (ϵ) is the proton (photon) energy and the proton and neutral pion masses are m_p and m_{π^0} , respectively. The CMB photon density is given by $n(\epsilon)$ in units of $\text{cm}^{-3} \text{eV}^{-1}$ and the photoproduction cross section, $\sigma_{p\gamma}(s)$, is taken from the parametrization implemented in SOPHIA.

The mean energy loss distance $x_{\text{loss}}(E)$, shown in Fig. 1a as triple-dot-dashed curve, is calculated as

$$x_{\text{loss}}(E) = \frac{E}{dE/dx} = \frac{\lambda(E)}{\kappa(E)} \quad (5)$$

with $\kappa(E)$ being the mean inelasticity

$$\kappa(E) = \frac{\langle \Delta E \rangle}{E}. \quad (6)$$

The mean energy loss of the nucleon due to the hadron production, $\langle \Delta E \rangle$, has been calculated by simulating 10^4 interactions for each given proton energy, resulting in a statistical error of the order of 1%. For $E > 10^{20}$ eV losses through photomeson production dominate with a loss distance of about 15 Mpc at $E \geq 8 \times 10^{20}$ eV. Below this energy, Bethe-Heitler pair production and adiabatic losses due to the cosmological expansion in the Hubble flow determine the proton energy losses.

Both the photoproduction interaction and the pair production are characterized by strongly energy dependent cross sections and threshold effects. Fig. 1a shows λ_{ph} decreasing by more than three orders of magnitude for a proton energy increasing by a factor of three. After the minimum λ_{ph} is reached, the proton energy loss distance is approximately constant. It is worth noting that the threshold region of λ_{ph} is very important for the shape of the propagated proton spectrum. As pointed out by Berezhinsky & Grigoreva [8], a pile-up of protons will be formed at the intersection of the photoproduction and pair production energy loss distances. Another, smaller pile-up will develop at the intersection of the pair production and adiabatic loss functions.

In the current calculation we treat pair production as a continuous loss process which is justified considering its small inelasticity of $2m_e/m_p \approx 10^{-3}$ (with m_e, m_p being the electron and proton masses, respectively) compared to pion-photoproduction ($\kappa \approx 0.2 - 0.5$). We use the analytical fit functions given by Chodorowsky *et al.* [28] to calculate the mean energy loss distance for Bethe-Heitler pair production. This result is in excellent agreement with results obtained by simulating this process via Monte Carlo as done by Protheroe & Johnson [12].

The turning point from pion production loss dominance to pair production loss dominance lies at $E \approx 6 \times 10^{19}$ eV, with a mean energy loss distance of ≈ 1 Gpc. The minimum of the pair production loss length is reached at $E \approx (2 - 4) \times 10^{19}$ eV. For $E \leq (2 - 3) \times 10^{18}$ eV continuous losses due to the expansion of the universe dominate. For an Einstein-de Sitter (flat, matter-dominated) universe as considered here, the cosmological energy loss distance scales with redshift z as

$$x_{\text{loss,ad}}(E, z) = \frac{c}{H_0} (1+z)^{-3/2} \approx 4000 \text{ Mpc} (1+z)^{-3/2}, \quad (7)$$

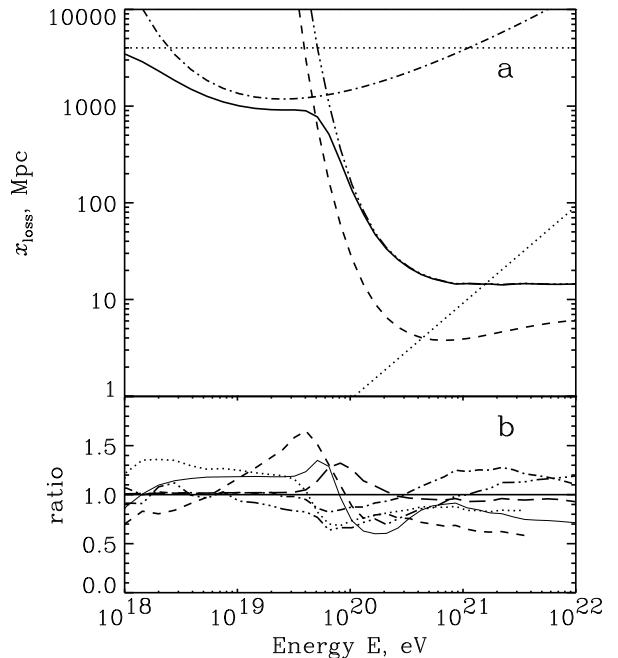


FIG. 1. a) Mean energy loss length due to adiabatic expansion (upper dotted curve), Bethe-Heitler pair production (dash-dotted curve), hadron production (triple-dot-dashed curve). Also shown are the hadron interaction length (dashed curve) and the neutron decay length (lower dotted curve). The solid line shows the total x_{loss} . b) Ratio of mean energy loss length as calculated in Refs. [8] (dotted), [10] (long-dashed), [9] (short-dashed), [12] (dash-dotted), [13] (dashed-dot-dot-dot), and [25] (thin solid) to the loss length of the present work presented in the upper panel.

for a Hubble constant of $H_0 = 75 \text{ km/s/Mpc}$, which we use throughout this paper. All other energy loss distances, $x_{\text{loss,BH}}$ for Bethe-Heitler pair production and $x_{\text{loss,ph}}$ for photomeson production, scale as

$$x_{\text{loss}}(E, z) = (1+z)^{-3} x_{\text{loss}}[(1+z)E, z=0]. \quad (8)$$

We also show the mean decay distance of $\sim 9 \times 10^{-9} \gamma_n \text{ kpc}$ for neutrons, where γ_n is the Lorentz factor of the neutron. Obviously, neutrons of energy below 10^{21} eV tend to decay, whereas at higher energies neutrons tend to interact.

Since the details of the proton energy loss directly affect the proton spectra after propagation, we present the ratio of the loss distance in previous calculations to that of our work on a linear scale in Fig. 1b. Generally all values of the energy loss distance are in a good qualitative agreement. Rachen & Biermann [10] treat both Bethe-Heitler and pion production losses very similarly to our work except for the threshold region of pion production. In the pair production region our work is also in perfect agreement with Protheroe & Johnson [12]. An overestimate of the loss distance due to pion production of $\sim 10 - 20\%$ in Ref. [12], however, will result in a small shift of the GZK cutoff to higher energies in comparison to the present calculations. Berezhinsky & Grigoreva [8] used a very good approximation for the pion production losses, but under-

estimate the energy loss in pair production interactions by at least 30-40%. The largest deviation of the combined loss distance from our model appears in the calculations of Yoshida & Teshima [9]. As already pointed out in Ref. [12] the largest difference occurs at $\approx 5 \times 10^{19}$ eV where Ref. [9] underestimates pair production losses and uses x_{loss} values larger by about 60%, while photoproduction losses are overestimated by up to 50%. In the work of Lee [13] pion as well as pair production losses are treated in fair agreement with our work, with differences up to 40% in the threshold region of pion production, and 10-20% otherwise. The energy loss code of Lee was also used by Sigl and collaborators [22,23]. The simple analytical estimate of photoproduction losses in the recent work of Achterberg *et al.* [24,25] underestimates the photoproduction loss distance by 10–40%, while x_{loss} due to pair production losses is overestimated by about 20%.

B. Method of particle propagation

UHECR propagation involves two main distance scales: (a) the hadronic interaction length λ_{ph} of typically 3 to 7 Mpc, and (b) the much smaller length scale ℓ_{mag} of typically 10 kpc needed for a precise numerical integration of the equations of motion in a random magnetic field. A straightforward Monte Carlo treatment of the propagation using a step size of ℓ_{mag} for both hadronic interactions and the equations of motion leads to severe efficiency problems for total propagation distances of hundreds of Mpc. Hence, the Monte Carlo simulation is done in the following way. First the path length X_{dist} from the current particle position to the next possible hadronic interaction is determined from

$$X_{\text{dist}} = -\lambda_{\text{ph},\text{min}} \ln(\xi), \quad (9)$$

where $\lambda_{\text{ph},\text{min}}$ is the minimum interaction length for hadronic interactions (at maximum redshift possible for a given total propagation distance) and ξ is a random number uniformly distributed in $(0, 1]$. The nucleon is then propagated over the path length X_{dist} in steps of ℓ_{mag} , and for charged particles Bethe–Heitler losses are taken into account and the deflection angle is calculated. A hadronic interaction is then simulated with the probability $\lambda_{\text{ph},\text{min}}/\lambda_{\text{ph}}(E, z)$, $\lambda_{\text{ph}}(E, z)$ being the interaction length for the energy E and redshift z . It is shown in Appendix A that this method corresponds exactly to a propagation simulation using Eq. (9) with $\lambda_{\text{ph}}(E, z)$ for the calculation of the interaction distance at each step with the length ℓ_{mag} .

The reduction of the proton energy due to BH pair production and of all nucleons due to adiabatic expansion is calculated at every propagation step, whereas the corresponding loss lengths are updated after a simulated path length of $\lambda_{\text{ph},\text{min}}$ and every photoproduction interaction. In the case of neutrons the decay path length is sampled using Eq. (9) with the neutron decay length. The smaller of both the hadronic interaction and the decay lengths determines then the larger scale of the simulation.

If a photoproduction interaction has occurred, the new energy of the proton (neutron) is substituted for the old one, and the energies and particle types of the secondary particles are recorded. The event generator SOPHIA generates the full set of secondary particles, including nucleon–antinucleon pairs. Thus the total flux of nucleons after propagation is slightly higher than the injected proton flux. Although this is not essential for the main results of this paper, it may occasionally affect the normalization of the proton arrival spectra.

The propagation is completed when the distance between the injection point and the particle location exceeds the predefined source distance. To obtain precise results for the time delay (e.g. total nucleon path length compared to the path length of a light ray), the last integration step is adjusted to end exactly at the desired distance.

Particles are injected at a point in space with a randomly chosen small angular deviation from the z -axis which defines the main propagation direction. The space along the z -axis is subdivided into $32 \times 32 \times 512$ cubes of side 250 kpc, each filled with a random magnetic field of average strength $\langle B \rangle = 10^{-9}$ Gauss (1 nG) [29] satisfying a Kolmogorov spectrum with three logarithmic scales. In practice three field vectors of random orientation are sampled at scales $\ell = 1000, 500$, and 250 kpc with amplitudes proportional to $\ell^{1/3}$ (see Appendix B). The final magnetic field in each of the 250 kpc cubes is the vectorial sum of these three vectors. Cyclic boundary conditions are imposed in case a particle leaves the space of pre-calculated magnetic fields. This means that the magnetic field experienced by a particle at location \mathbf{x} is the same as the field calculated at \mathbf{x}' ,

$$x'_i = x_i - N_i R_i, \quad i = x, y, z \quad (10)$$

with R_i being the size of the pre-calculated magnetic field region in direction i . N_i is the largest integer number satisfying $x_i - N_i R_i \geq 0$. The magnetic field values are refreshed after the calculation of 100 propagations to exclude systematic effects by our choice of field vectors. We have verified numerically that the magnetic field constructed in this way obeys approximately $\text{div}(\mathbf{B}) = 0$ and that recalculations of the field at smaller intervals do not change the final result. We assume that the magnetic field strength does not scale with redshift. More information about the implementation of the random magnetic field is given in Appendix B.

The value chosen for ℓ_{mag} , in principle, depends strongly on the average magnetic field and nucleon energy, and is a compromise between the precision of the calculation and computing time limits. We have chosen $\ell_{\text{mag}} = 10$ kpc for $\langle B \rangle = 1$ nG, with an inverse linear scaling for other B values. A step size of 1 kpc has been used for short distance propagations to ensure accurate results for arrival angle and time delay distributions.

Finally, it should be mentioned that the calculation of the redshift at a given distance can be done only approximately. The reason is the unknown total travel time of a particle from the source to Earth at injection time. The actual travel time (path length) can be significantly larger than the light travel time along a geodesic and is, in general, different for each simulated particle trajectory. In the following we use the proper

distance-redshift relation to define the redshift of the source and along the travel path at observation time. This approximation does not strongly affect our results since we consider here mainly distances with redshifts smaller than 0.06 and weak magnetic fields. However, it should be noted that, in the case of a strong magnetic field, cosmological evolution might become important already at relatively short distances.

III. RESULTS AND COMPARISON WITH PREVIOUS WORK

In this section, we present results from the simulation of proton propagation. We start with mono-energetic proton fluxes for which we can compare our results with previous work, and which reflect more directly the different treatments of the energy loss processes. We then compare results for the propagation of protons injected with a power law spectrum.

One can divide previous calculations into two general groups: Monte Carlo based methods, like our own one, and analytical/numerical calculations. Protheroe & Johnson [12] have used a matrix technique to follow the particles over cosmological distances and calculate the γ -ray, neutrino and nucleon spectra arriving at Earth. The energy loss matrices for all particles are calculated with Monte Carlo event generators. We have compared our SOPHIA event generator with the one of Ref. [12] by propagating with the same method an E^{-2} proton spectrum with different exponential cutoffs (see Eq. (11)). For this purpose we have used SOPHIA and the event generator of Ref. [12] to calculate the corresponding photoproduction matrices and have applied the two matrices to propagation over the same set of distances. A comparison of the resulting secondary particle spectra yields excellent agreement, pointing to a similar treatment of the particle production process in the different codes. We have also compared the matrix method with our Monte Carlo approach by propagating an exponentially modified power law injection spectrum over 200 Mpc. Again good agreement is found for the resulting ν_μ -spectra, while the $\bar{\nu}_e$ - and neutron spectra are at variance with our calculations, which we attribute to a different treatment of the neutron decay. Also, our Monte Carlo method results in more losses due to pair production for distances ≥ 200 Mpc and a sharp spike at the injection energy for very short distance propagation, a consequence of the Poisson nature of photon-proton encounters. This feature is discussed in detail in Sect. III.A.

The approach used by Berezhinsky & Grigoreva [8] and Rachen & Biermann [10] is to solve the transport equation quasi-analytically by approximating the collisional terms as continuous energy loss terms. This does not take into account the Poissonian nature of the pion production process as pointed out above, and introduces artifacts into the resulting nucleon spectra in form of sharp pile-ups. Lee [13] used a numerical technique to solve the transport equation for particle propagation without using the continuous loss approximation.

The common assumption in all this work is to consider the spatial propagation as strictly along a null-geodesic, with the

consequence of not being able to gain knowledge about time delays and arrival angles of the cosmic rays with respect to light and neutrino propagation.

A hybrid model, combining a Monte Carlo particle transport code with analytical techniques was presented by Achterberg *et al.* [24]. Besides simplifying the properties of the energy losses by analytical estimates (see Fig. 1b), this code also describes the scattering in the magnetic field as a diffusion process employing stochastic differential equations. This approach has the advantage to allow large propagation steps, and is thus computationally very fast, but has a disadvantage at small propagation distances which we discuss further below. Our approach is to use the Monte Carlo technique for simulating particle production and to follow closely cosmic ray orbits in 3D-magnetic field configurations while traveling through the nearby Universe to Earth. This concept, while being the most accurate one, limits our propagation calculation to small source distances.

A. Propagation of mono-energetic protons

In this section we present distributions of arrival energy, arrival direction and time delay of the nucleons, as well as neutrino spectra, for mono-energetic injection of protons at distances of 2, 8, 32, 128 and 512 Mpc from Earth. Protons are injected with energy $10^{21.5}$ eV. At this energy, propagated protons can easily suffer several photoproduction interactions, and this tends to emphasize the pion production features.

Fig. 2 shows the distribution of arrival energy of protons and neutrons. Clearly visible is the effect of the statistical nature of photon-proton encounters, also found qualitatively in Ref. [24]. At a distance of 2 Mpc, roughly 60% of all injected particles do not interact, and this generates a sharp spike at the injection energy. This effect due to Poisson statistics remains visible for distances up to ~ 30 Mpc, showing up as a high-energy spike in the cosmic ray spectrum. At larger distances, essentially all injected particles undergo interactions, and therefore, the high-energy spike vanishes. The arrival energy distributions then become much narrower, and in propagation over larger distances would scale simply with the energy loss distance for pair production and adiabatic losses, modified by the increasing scattering in the magnetic field.

Fig. 3 shows the distribution of the average time delay of the cosmic rays arriving at Earth with respect to propagation along a geodesic with the speed of light. This delay is caused by scattering of the charged particles by the intergalactic magnetic field, leading to an increase of the particle's effective path length. Thus, the average time delay increases with propagation distance, as visible in Fig. 3. Like the arrival energy distributions, the distributions of the time delay also show signs of Poisson statistics, visible especially when propagating over short distances.

The time delay effectively reflects the arrival energy distribution $t_{\text{del}} \propto 1/E_{\text{arr}}^2$ as a result of the random walk process [20,24]. This also emphasizes the importance of an accurate treatment of energy losses. For example, a direct com-

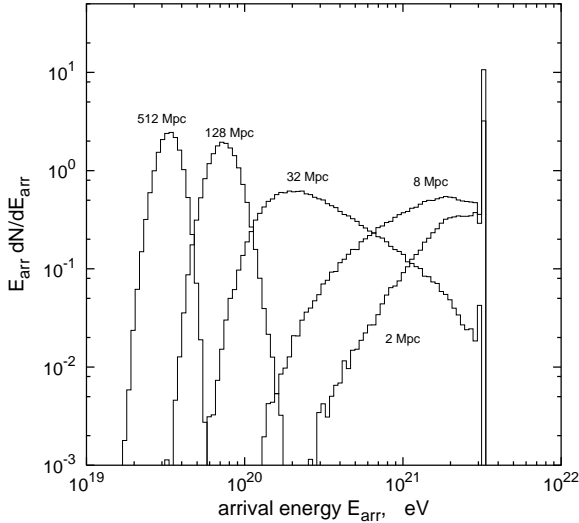


FIG. 2. Arrival spectrum at Earth for mono-energetic injection of protons of energy $E = 10^{21.5}$ eV and for various source distances as indicated. The sharp spike at injection energy for distances $D \leq 32$ Mpc is due to the low interaction probability within the short distance.

parison with the propagation code of Achterberg *et al.* [24,25] for (almost) the same propagation parameters has shown differences in the time delay up to one order of magnitude for $D = 32$ Mpc. For the same propagation distance, the code by Achterberg *et al.* produces a peak in the arrival energy distribution about a factor of 2 lower than found in the present work, due to its 20% overestimation of energy losses in the photoproduction regime. Together with a difference in the magnetic field sampling, which leads to an effective correlation length $\ell_{\text{corr}} \approx 390$ kpc for the Kolmogorov spectrum used in the present work (see Appendix B) compared to $\ell_{\text{corr}} = 1$ Mpc for the homogeneous cell approach used in Ref. [24], the observed differences can then be fully understood by the relation $t_{\text{del}} \propto \ell_{\text{corr}}/E_{\text{arr}}^2$, as derived in Ref. [24].

Protons with injection energy $\leq 10^{19}$ eV suffer mainly continuous BH pair production and adiabatic losses that are proportional to their path length. The substantial deflection in the random magnetic field at such energies results in a significant increase of the path length. For protons injected at a sufficiently large distance this can also lead to excessive time delays. For example, cosmic rays with energy of about 10^{19} eV, injected at distances greater than 500 Mpc in a 1 nG magnetic field, show a time delay exceeding the Hubble time. This gives a strict constraint on the cosmic ray horizon.

The diffusion coefficient for an effective description of the scattering process in the magnetic field is strongly energy dependent, and so is the time delay, t_{del} . To emphasize this correlation, and demonstrate the advantages of the Monte Carlo approach, we show in Fig. 4 the scatter plot of proton energy versus delay after propagation over 32 Mpc. There is a strong correlation suggesting that energy changes of one and a half orders of magnitude lead to differences in delay times of more

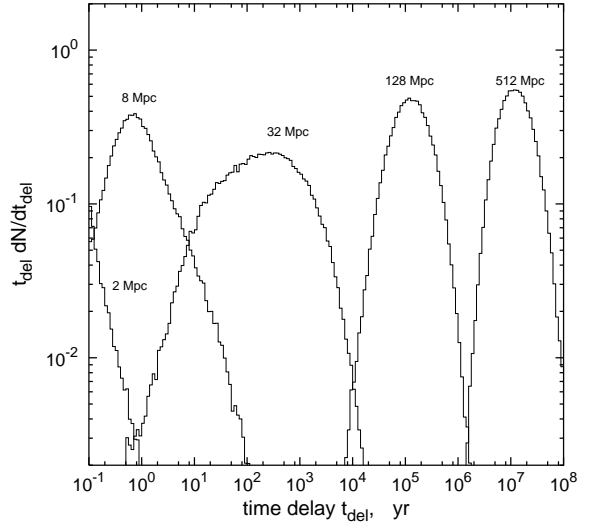


FIG. 3. Time delay of protons injected at different source distances and propagated through a random magnetic field of 1 nG. The time delay is defined as the propagation time of a particle minus the travel time of a light ray along a geodesic.

than three orders of magnitude, i.e. we find an energy dependence similar to $\langle t_{\text{del}} \rangle \propto (BD/E)^2$ as derived by Achterberg *et al.* [24] in the small scattering-angle approximation and the quasi-linear approximation of wave-particle interactions. The correlation becomes less pronounced when propagating over significantly larger distances simply because the arrival energy distributions become much narrower and the statistical nature of the energy loss is smoothed by the prevailing pair production and adiabatic losses. This correlation, however, would have very important implications for specific models of UHECR production, where the duration of an active phase of the source competes with the time delay of the protons during propagation. The extreme case would be the acceleration of UHECR in gamma ray bursts. The particles with the highest energies are expected to arrive first, followed by a dissipating widening halo of lower energy protons, as emphasized by Waxman & Miralda-Escudé [18].

For large propagation distances, even protons injected with $10^{21.5}$ eV show time delays that are a considerable fraction of the light propagation time (5–10% for 512 Mpc). This would lead to a limiting proton horizon for a large set of source distances and magnetic field values [24]. 512 Mpc is already a limiting horizon for protons injected with 10^{19} eV in 1 nG fields, as noted above.

The scattering that leads to time delay also causes angular deviations from the direction to the source, as shown in Fig. 5 for the injection of mono-energetic protons at the same set of distances. Note that in our propagation code the ‘observer’ sits on a sphere surrounding the injection point. The angle shown is the angle between the particle’s arrival direction and direction to the injection point. This ‘arrival angle’ is somewhat different from the angle between particle’s arrival direction and the injection direction. This method may lead to an

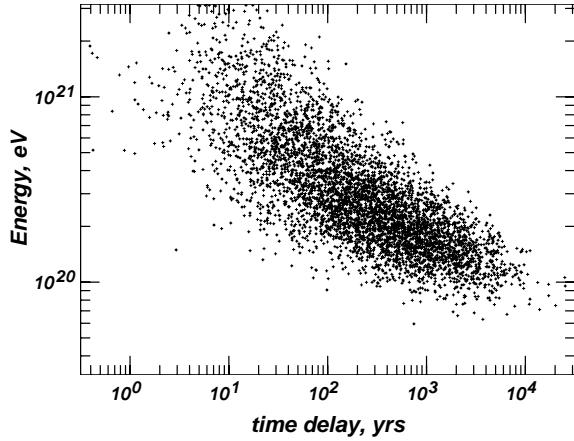


FIG. 4. Scatter plot of time delay versus energy for protons injected with energy of $10^{21.5}$ eV after propagation over 32 Mpc in random B field of 1 nG.

underestimate of the scattering angle and the time delay when the particle fluxes become nearly isotropic and many particles have a high probability to scatter back through the ‘observer’s sphere’. It will not, however, affect strongly the results presented in this paper, because, as Fig. 5 demonstrates, we do not reach the limit of isotropic 3D diffusion.

The features of the angular distribution closely follow the time delay distributions already shown. For large propagation distances, the cosmic ray arrival directions are distributed uniformly up to a maximum deflection angle, which increases with propagation distance to reach more than 20° at 512 Mpc. At propagation distances smaller than ~ 30 Mpc, thus a few times the proton interaction length λ_{ph} , a peak at small deflection angles occurs due to the effect of Poisson statistics for proton–photon interactions.

Finally Fig. 6 shows the electron and muon neutrino spectra generated by the injection of $10^{21.5}$ eV protons at the same set of distances. The muon neutrino spectra develop as a function of the proton arrival energy spectra folded with the photoproduction cross section. The fluxes grow with propagation distance, and the maximum neutrino energy shifts to lower energy reflecting the decreasing proton energy. The growth rate with distance decreases for very large distances, where the average proton energy significantly decreases and λ_{ph} is correspondingly significantly longer.

Electron neutrino spectra show another, very interesting feature, that develops with distance. At a minimum distance of 2 Mpc the ν_e -flux reaches its maximum of 1/2 of the ν_μ spectrum and shows a somewhat wider energy spectrum, enhanced at low energy. At larger distances an additional ν_e component develops at significantly lower energy. As already noted in Ref. [9], these are $\bar{\nu}_e$ ’s from neutron decay. The resulting protons from the decay process carry most of the energy, leaving for the $\bar{\nu}_e$ ’s an average energy of only $\approx 5 \times 10^{-4}$ of the original neutron energy, and the ν_e -peak is placed at about two orders of magnitude to lower energy with respect

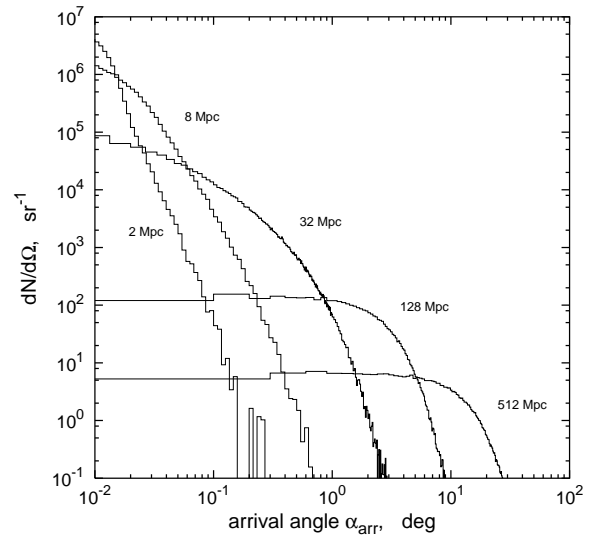


FIG. 5. Angular distribution of the arrival angle at Earth for mono-energetic injection of protons of energy $E = 10^{21.5}$ eV, and for various source distances as indicated. The magnetic field is 1 nG.

to the ν_μ -peak. The strength of this component increases with distance relative to the direct ν_e component from μ^\pm decay.

B. Cosmological modification of the cosmic ray source spectrum

Berezinsky & Grigoreva [8] introduced the modification factor $M(E, z)$ to represent the cosmological evolution of the UHECR spectra. $M(E, z)$ gives the ratio of propagated to injected protons at the same energy E , for a fixed injection spectrum, as a function of the redshift of the injection distance compensating for the proton adiabatic losses. $M(E, z)$ is thus exactly unity for proton energies below the $p\gamma$ -particle production energy threshold.

At the highest injection energies the modification factor shows the GZK cutoff, followed by a pile-up at the crossover of photoproduction and pair production energy loss. This pile-up is a direct consequence of the resonance nature of photoproduction and the hadronic particle production threshold. The next feature at still lower energy is a shallow dip corresponding to the pair production loss, followed by a small pile-up below it. The magnitude of the pile-ups and dips depend not only on the distance and the mean loss distance at the photoproduction/pair production crossover, but also on the shape of the proton injection spectrum. Flatter spectra create bigger pile-ups, because of the increased number of higher energy protons that have interacted to lose energy. The pile-up energy is linked to the energy where losses due to pair production take over from pion production losses, and is therefore strongly dependent on the details of the loss processes in the simulations. Fig. 7a shows $M(E, z)$ for propagation without magnetic field for the sole reason of comparison with previous work. An E^{-2} proton spectrum with a sharp cutoff at

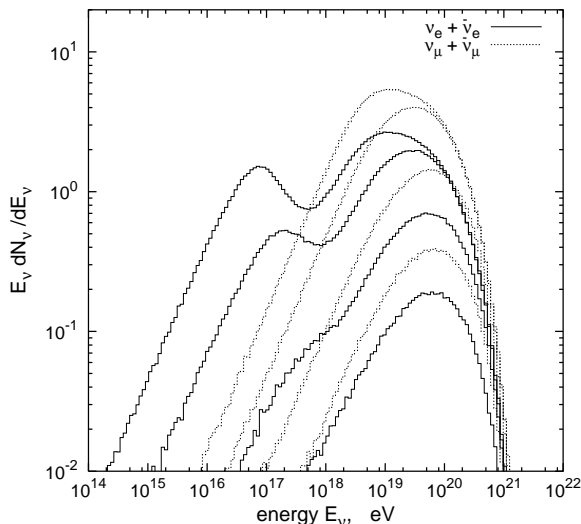


FIG. 6. $\nu_\mu + \bar{\nu}_\mu$ and $\nu_e + \bar{\nu}_e$ -spectra at Earth after propagating a mono-energetic proton beam of energy $10^{21.5}$ eV at distances of 2, 8, 32 and 128 Mpc (from bottom to top) in a 1 nG intergalactic magnetic field.

$E_c = 3 \times 10^{20}$ eV is injected, and we propagate over a distance of 256 Mpc in our calculation (solid line) compared to Refs. [10] (dotted line, $D=240$ Mpc), [12] (dashed-dotted line, $D=256$ Mpc), [9] (dashed line, $D=228$ Mpc, $E_c = 10^{20}$ eV) and [13] (dashed-dot-dot-dot line, $D=256$ Mpc). There is excellent agreement at all energies with the work of Protheroe & Johnson [12]. The sharp photoproduction peak of Rachen & Biermann [10] is an artifact coming from their continuous loss approximation for pion photoproduction. As noted previously, Yoshida & Teshima [9] used a loss curve which shows a significant deviation from that used in the present paper, and hence their corresponding pile-up height is also larger than in our work. We agree with the position of the pile-up of Lee [13]. However, due to an overestimate of the loss rate at this energy, the magnitude of the pile-up in this paper is smaller than in our model. The dip just below the pile-up is in reasonable agreement with all other works.

Fig. 7b illustrates the effect of scattering in the magnetic field by comparing the resulting corresponding modification factors. The ‘no scattering’ curve (dashed line, as in Fig. 7a) is much higher than the more realistic ‘scattering curve’ in the energy range between 10^{18} and 10^{19} eV. The reason is that particles in this energy range have considerable time delays and correspondingly much higher total energy loss in pair production interactions. Another consequence of the increased proton travel time due to scattering is the development of a higher pile-up at about 10^{18} eV, corresponding to the large number of particles moved to lower energies from the region of that dip. Note that simulation of 10^{18} eV particles in a 1 nG field is at the threshold of our direct Monte Carlo approach, and the calculation is not carried to lower energy where it might show an additional pile-up content. Fig. 7b thus demonstrates the importance of the proton scat-

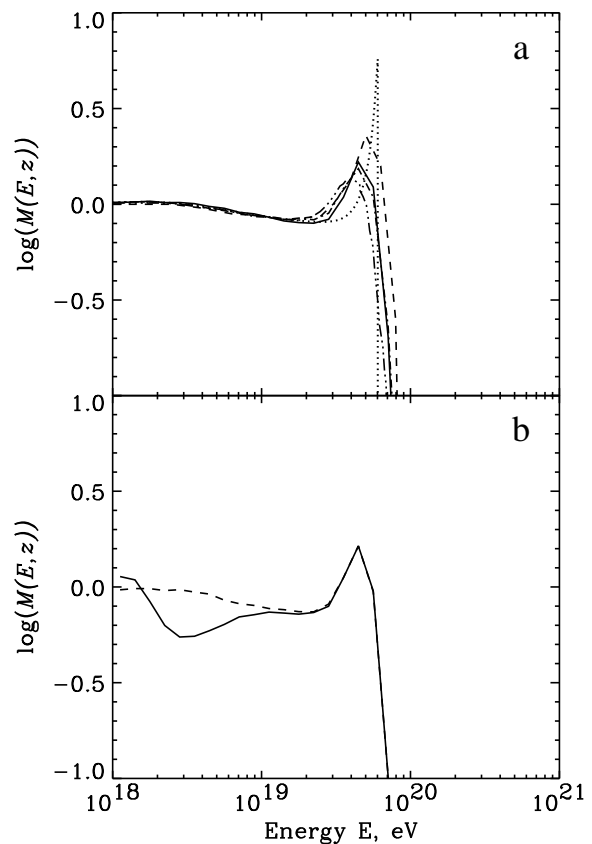


FIG. 7. Upper panel: modification factors for propagation over a distance of 256 Mpc without magnetic field after injection of a E^{-2} proton spectrum with a sharp cutoff at $E_c = 3 \times 10^{20}$ eV. This calculation (solid line) is compared to Refs. [10] (dotted line, $D=240$ Mpc), [12] (dashed-dotted line, $D=256$ Mpc), [9] (dashed line, $D=228$ Mpc, $E_c = 10^{20}$ eV) and [13] (dashed-dot-dot-dot line, $D=256$ Mpc). Lower panel: comparison of the modification factor for rectilinear propagation (dashed curve, ‘no scattering’ curve) and for propagation in a 1 nG magnetic field (solid line, ‘scattering curve’) including the effect of scattering.

tering in the extragalactic magnetic fields for the shape of the final spectrum on arrival at Earth.

It is important to note that the curves shown in Fig. 7b are calculated for a source with unlimited lifetime. In addition, by construction, energy loss due to cosmological evolution does not enter the modification factor $M(E, z)$. Imposing a constraint on the source lifetime will change the modification factor considerably for low energies because, for a given distance, the time delay due to the scattering in the turbulent magnetic field might become comparable to or even exceed the source lifetime.

IV. FORMATION OF THE PRIMARY AND SECONDARY PARTICLE SPECTRA DURING PROPAGATION

To study the development of the primary and secondary particle spectra we followed the propagation of protons injected

with a E^{-2} power law spectrum with an exponential cutoff at $10^{21.5}$ eV, i.e.

$$\frac{dN}{dE} = AE^{-2} \exp[-E/(10^{21.5} \text{ eV})]. \quad (11)$$

We recorded the spectra after propagation over 10 Mpc intervals up to a source distance of 200 Mpc. The results of this calculation are relevant for models of UHECR acceleration at astrophysical shock fronts, although the cutoff energy adopted in this calculation is fairly high. 10,000 protons were injected with a power law spectrum (integral spectral index $\gamma = 1$) in each of 30 energy bins covering energies from 10^{19} to 10^{22} eV, i.e. 10 bins per decade of energy. We did not simulate the propagation of lower energy particles, which do not experience photoproduction interactions, but followed the secondaries down to arbitrary low energies.

Fig. 8a shows the evolution of the particles injected in the highest energy bin $10^{21.9}$ to 10^{22} eV. The size of each rectangle is proportional to the fractional energy distribution after propagation over 10, 20, etc., Mpc. The rate of energy degradation is dramatic. After only 10 Mpc the spectrum of protons injected in a 0.1 logarithmic bin have spread over one and a half orders of magnitude. The width of the energy distribution increases with the propagation distance up to ~ 30 Mpc and then decreases. Qualitatively this behavior is very similar to the calculation of Aharonian & Cronin [11], although the direct comparison is difficult because of the different approach to the calculation. The average behavior of all protons injected with energy above about 3×10^{20} eV is similar, although the magnitude of the spread decreases — particles of energy below 10^{20} eV suffer much smaller losses. After propagation over about 100 Mpc the spectrum shown in Fig. 8 is already final - it is concentrated within roughly 1/2 order of magnitude around $\sim 8 \times 10^{19}$ eV. This energy slowly decreases because of pair production and adiabatic losses during propagation over larger distances, but without change in the shape of the distribution.

The lower panel of Fig. 8 shows the fractional energy carried by different particles after propagation in terms of the total energy of the protons injected with energy spectrum described by Eq. 11. The proton curve, which also includes neutrons, always dominates. The energy content in protons, however, is only about 50% of that injected for distances above 120 Mpc. The rest of the injected energy is distributed between the electromagnetic component and neutrinos. Note the difference between the photon (and electron) components from photoproduction (long dashed line), and from pair production (short dashed line). While the photoproduction component rises very quickly and changes very little after 100 Mpc, the pair production component is almost proportional to the distance, as most of the injected protons, despite the high threshold of 10^{19} eV, have similar pair production losses. At distances of 100 (200) Mpc 51% (43%) of the injected power is carried by nucleons, 31% (37%) by the electromagnetic component and 18% (20%) by neutrinos. The neutrino fluxes will remain at the same level during propagation over larger distances, and the established energy balance will only slightly change as nucleons yield some of their

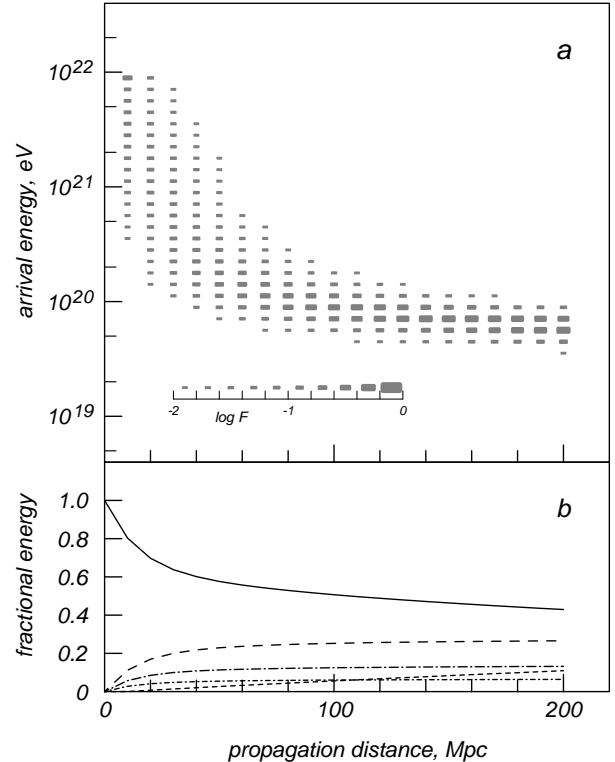


FIG. 8. a) Arrival energy distribution for protons injected with energy between $10^{21.9}$ and 10^{22} eV after propagation on 10, 20, ... 200 Mpc. b) Fractional energy contained in nucleons (solid line), γ -rays from photoproduction (long dashes) and BH pair production (short dashes) for protons injected with the energy spectrum of Eq. 11. The dash-dot lines show the fractional energy in muon (long) and electron (short) neutrinos and antineutrinos.

power to the electromagnetic component through pair production. Adiabatic losses will, of course, affect all components in the same way.

In addition to distributing a fraction of the energy of the injected protons to secondary particles, the propagation changes the energy spectrum of protons. The most energetic nucleons lose energy fast and are downgraded after a short propagation distance. The number of nucleon with energy above 10^{21} eV decreases by 10%, 50% and 90% from the injected number of protons after only 1, 6, and 20 Mpc. The corresponding distances for nucleons of energy above 10^{20} eV are 10, 40 and 85 Mpc. The magnitude of these changes emphasizes the importance of detection of very high energy particles: for particles of energy above 3×10^{20} eV (same as the highest energy event detected by the Fly's Eye [30]) these distances are 1, 10 and 30 Mpc. The rapid absorption of the highest energy cosmic rays implies that the horizon of the highest energy protons is very small, and increases the energetics requirements for potential UHECR sources.

V. DISCUSSION, CONCLUSIONS AND OUTLOOK

The Monte Carlo propagation of ultra high energy protons in a random extragalactic magnetic field has obvious advantages over other approaches to calculations of proton propagation in the cosmologically nearby Universe. To start with, this approach takes fully into account fluctuations in the positions of proton interactions, and thus also in the proton energy losses and production of secondary particle fluxes. It also naturally generates the correlations between the proton's arrival energy, its time delay, and its angular deviation from the source direction. We have also shown that mathematical approaches which use a diffusion description of magnetic scattering, although superior in computational speed, can lead to significant systematic errors for propagation distances smaller than ~ 100 Mpc.

These features of the calculation become extremely valuable when applied to specific models of UHECR acceleration, especially models that involve a relatively short (compared to light travel time and proton time delay) active phase of the source. An extreme example for such a model is the GRB model for UHECR acceleration. However, other models involving interacting galaxies or radio galaxies of specific morphology could also be affected, especially if embedded in regions of high (random) magnetic field.

At energies that allow protons to photoproduce, namely above 10^{20} eV, the energy degradation is extremely rapid. This is not very surprising because of the very short photoproduction interaction length at energies corresponding to the maximum cross section – i.e. λ_{ph} below 4 Mpc for energies between 4×10^{20} eV and 10^{21} eV. This energy range is very relevant, as it is just above the highest energy particles detected by the Fly's Eye and AGASA arrays [30,2]. A large part of this rapid energy dissipation in our calculation is due to the correct implementation of the fluctuations in photoproduction interactions in SOPHIA. A good example for the size of the fluctuations is the proton energy distribution after propagation over 10 Mpc shown in Fig. 8, which covers more than one and a half orders of magnitude. This is an extreme case. However, every particle injected with an energy well above the photoproduction threshold would very rapidly result in a distribution extending down to the threshold, within the first 10 Mpc.

This rapid energy dissipation creates additional problems for models of cosmic ray acceleration at astrophysical shocks. Apart from the difficult question of the maximum acceleration energy, such models require that a significant fraction (0.01 to 0.1) of their source luminosity contributes to the UHECR flux. The rapid energy dissipation increases the energy requirements in terms of total luminosity and severely limits the source distance. Because of magnetic scattering, such limits could also be set for particles injected with energy below the photoproduction threshold.

Fig. 9 shows the 50% horizon for UHECR sources as a function of source particle energy for $\langle B \rangle$ values of 0.1, 1 and 10 nG. The 50% horizon R_{50} is defined here as the light propagation distance to the source at which $1/e$ of all injected

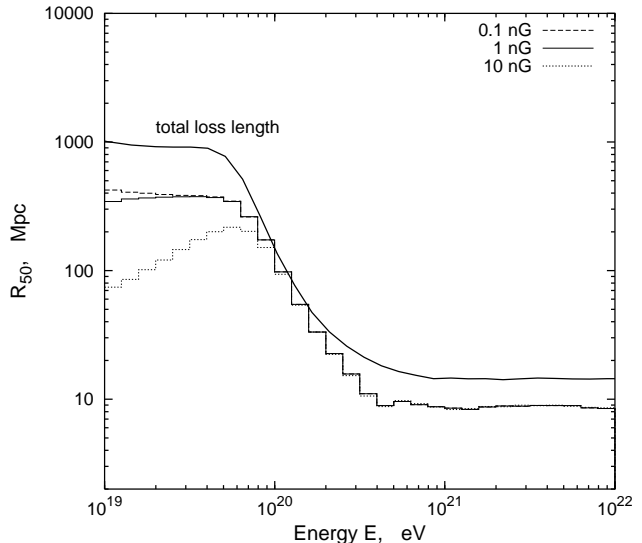


FIG. 9. Proton 50% horizon as a function of injection energy for average random magnetic fields of 0.1 (dashed histogram), 1 (solid histogram), and 10 (dotted histogram) nG. See text for definition. The solid line is the total energy loss length from Fig. 1, shown here for comparison.

protons have retained 50% or more of their energy, i.e. R_{50} is achieved when

$$\int_{\frac{E_0}{2}}^{E_0} \frac{dN}{dE} dE = N_0 \exp(-1), \quad (12)$$

where N_0 is the number of particles injected with energy E_0 .

To start with, R_{50} is small at any energy, and demonstrates the resonant nature of the photoproduction cross section. At $E = 10^{20}$ eV R_{50} is about 100 Mpc, while at 2×10^{20} eV it decreases to 20 Mpc and becomes smaller than 10 Mpc for energies above 3×10^{20} eV. For injection energies above 10^{20} eV the horizon energy dependence is similar to that of the energy loss distance shown in Fig. 1. These protons are not affected much by the magnetic field since their scattering angles are small, but suffer mainly from energy degradation due to $p\gamma$ encounters. Below 10^{20} eV the picture changes. The scattering in the magnetic field increases the propagation time and thus causes additional energy loss and an increase of the ratio x_{loss}/R_{50} .

Stronger magnetic fields create delays, that could be longer than the light propagation time from the source and reverse the trend – the horizon starts decreasing below $\sim 6 \times 10^{19}$ eV and is restricted to 75 Mpc at 10^{19} eV. Since the average time delay is inversely proportional to E^2 , the decrease of R_{50} is expected to become more drastic at lower energy. One consequence of the strong energy dependence of R_{50} is, for example, that our attempts to correlate the arrival directions of UHECR with different types of astrophysical objects should use only objects within the particle horizon depending on the magnetic fields strength in different regions of the Universe. Independently of the magnetic field value, however, the horizon defined above is much smaller than the conventional num-

bers of 50 or 100 Mpc for the highest energy cosmic ray events.

There are many relevant astrophysical problems which can be studied with the approach described in this paper. We plan to use the code for proton propagation in regular magnetic fields associated with large scale structures (local supercluster, supergalactic plane). The regular fields, especially if they reach the observationally allowed limits of $0.03 \mu\text{G}$ and even $0.1 \mu\text{G}$, could change the propagation patterns for 10^{19} eV cosmic ray protons and alter the horizon values shown in Fig. 9. We also plan to set limits on models of slow UHECR acceleration on shocks of very large dimensions and to look for possibilities of ultra-high energy γ -ray halos around the sources and along the tracks of the UHECR protons.

ACKNOWLEDGMENTS

The authors are indebted to A. Achterberg and the authors of Ref. [24] for sharing their corrected results prior to publication, and to P.P. Kronberg for careful reading of the manuscript and valuable discussions. The research of TS is supported in part by NASA Grant NAG5-7009. RE is supported in part by the US Department of Energy contract DE-FG02 91ER 40626. The work of RJP and AM was supported in part by a grant from the Australian Research Council. JPR is supported through the TMR network Astro-Plasma Physics, funded by the EU under contract FMRX-CT98-0168. AM thanks BRI for its hospitality during her visit. These calculations are performed on DEC Alpha and Beowulf clusters funded by NSF grant PHY-9601834.

[1] T. Abu-Zayyad *et al.*, Proc. 26th Int. Cosmic Ray Conf. (Salt Lake City, Utah), eds. D. Kieda, M. Salamon & B. Dingus, **3**, 264 (1999).
[2] M. Takeda *et al.*, *Phys. Rev. Lett.* **81**, 1163 (1998).
[3] A.M. Hillas, *Ann. Rev. Astron. Astrophys.* **22**, 425 (1984).
[4] A. Bhattacharjee & G. Sigl, *Phys. Rep.* to be published, *astro-ph/9811011*.
[5] G. Cocconi, *Nuovo Cimento*, **3**, 1433 (1956).
[6] K. Greisen, *Phys. Rev. Lett.* **16**, 748 (1966); G.T. Zatsepin & V.A. Kuzmin, *JETP Lett.* **4**, 78 (1966).
[7] C.T. Hill & D.N. Schramm, *Phys. Rev. D***31**, 564 (1985).
[8] V.S. Berezinskii & S.I. Grigoreva, *Astron. Astrophys.* **199**, 1 (1988).
[9] S. Yoshida & M. Teshima M., *Progr. Theor. Physics* **89**, 833 (1993).
[10] J.P. Rachen & P.L. Biermann, *Astron. Astrophys.* **272**, 161 (1993).
[11] F.A. Aharonian & J.W. Cronin, *Phys. Rev. D***50**, 1892 (1994).
[12] R.J. Protheroe & P.A. Johnson, *Astropart. Phys.* **4**, 253 (1996); erratum *ibid.* **5**, 215 (1996)
[13] S. Lee, *Phys. Rev. D***58**, 043004 (1998).

[14] T. Abu-Zayyad *et al.*, Proc. 26th Int. Cosmic Ray Conf. (Salt Lake City, Utah), eds. D. Kieda, M. Salamon & B. Dingus, **5**, 349 (1999).
[15] M. Boratav *et al.*, Proc. 25th Int. Cosmic Ray Conf. (Durban) eds. M.S. Potgieter, B.C. Raubenheimer & D.J. van der Walt, **5**, 205 (1997).
[16] T. Aoki *et al.*, Proc. 26th Int. Cosmic Ray Conf. (Salt Lake City, Utah), eds. D. Kieda, M. Salamon & B. Dingus, **5**, 352 (1999).
[17] L. Scarsi *et al.*, Proc. 26th Int. Cosmic Ray Conf. (Salt Lake City, Utah), eds. D. Kieda, M. Salamon & B. Dingus, **2**, 384 (1999).
[18] E. Waxman & J. Miralda-Escudé, *Astrophys. J.* **472**, L89 (1996).
[19] R. Lampard, R.W. Clay & B.R. Dawson, *Astropart. Phys.* **7**, 213 (1997).
[20] R.W. Clay *et al.* *Astropart. Phys.* **9**, 221 (1998).
[21] G.A. Medina Tanco, E.M. de Gouveia dal Pino, & J.E. Horvath, *Astropart. Phys.* **6**, 337 (1997).
[22] G. Sigl, M. Lemoine, & A.V. Olinto, *Phys. Rev. D***56**, 4470 (1997).
[23] G. Sigl, M. Lemoine, & P. Biermann, *Astropart. Phys.* **10**, 141 (1999).
[24] A. Achterberg, Y. Gallant, C.A. Norman & D.B. Melrose, *astro-ph/9907060*
[25] The preprint of Ref. [24] contains an error in the calculation of the energy loss distance, which will be corrected in a revised version (private communication with the authors). Our comparison is based on calculations performed after the correction of this error.
[26] A. Mücke *et al.*, *Comp. Phys. Comm.*, **124**, 290 (2000).
[27] R.J. Protheroe & P.L. Biermann, *Astropart. Phys.* **6**, 45 (1996).
[28] M.J. Chodorowski, A.A. Zdziarski & M. Sikora, *Astrophys. J.* **400**, 181 (1992).
[29] P.P. Kronberg, *Rep. Progr. Phys.* **57**, 325 (1994).
[30] D.J. Bird *et al.* *Astrophys. J.* **441**, 144 (1995).
[31] A.N. Kolmogorov, *C.R. Acad. URSS*, **30**, 201 (1941).
[32] P.L. Biermann & P.A. Strittmatter, *Ap. J.*, **322**, 643 (1987).

APPENDIX A: MONTE CARLO SAMPLING OF INTERACTION POINTS

In the following we discuss the application of the veto algorithm to the sampling of interaction points along a nucleon propagation path. The probability of having no hadronic interaction with a photon of the CMB within a path length interval (s_1, s_2) reads

$$P_{\text{no}}(s_1, s_2) = \exp \left\{ - \int_{s_1}^{s_2} \frac{ds}{\lambda_{\text{ph}}(E(s))} \right\}. \quad (\text{A1})$$

The interaction length itself depends only on the nucleon energy. However, because of the treatment of Bethe-Heitler losses as continuous process, this energy depends on the path length s . Correspondingly, the probability for one interaction in the interval $(s, s + ds)$ is given by

$$P_{\text{int}}(s)ds = P_{\text{no}}(0, s) \frac{ds}{\lambda_{\text{ph}}(E(s))}, \quad (\text{A2})$$

where $P_{\text{no}}(0, s)$ is the probability that no interaction has occurred before. In our approach we replace $\lambda_{\text{ph}}(E(s))$ by the constant $\lambda_{\text{ph, min}}$ and use (A2) to sample the path length distance from the current location ($s = 0$) to the next interaction. This interaction point is then accepted with the probability $\lambda_{\text{ph, min}}/\lambda_{\text{ph}}(E(s))$. Hence the interaction probability can be written as

$$P_{\text{int}}(s)ds = \left[\tilde{P}_{\text{no}}(0, s) + \int_0^s \frac{ds_1}{\lambda_{\text{ph, min}}} \tilde{P}_{\text{no}}(0, s_1) \left(1 - \frac{\lambda_{\text{ph, min}}}{\lambda_{\text{ph}}(E(s_1))}\right) \tilde{P}_{\text{no}}(s_1, s) + \int_0^s \frac{ds_1}{\lambda_{\text{ph, min}}} \tilde{P}_{\text{no}}(0, s_1) \left(1 - \frac{\lambda_{\text{ph, min}}}{\lambda_{\text{ph}}(E(s_1))}\right) \times \int_{s_1}^s \frac{ds_2}{\lambda_{\text{ph, min}}} \tilde{P}_{\text{no}}(s_1, s_2) \left(1 - \frac{\lambda_{\text{ph, min}}}{\lambda_{\text{ph}}(E(s_2))}\right) \tilde{P}_{\text{no}}(s_2, s) + \dots \right] \left(\frac{\lambda_{\text{ph, min}}}{\lambda_{\text{ph}}(E(s))}\right) \frac{ds}{\lambda_{\text{ph, min}}}, \quad (\text{A3})$$

where we have used

$$\tilde{P}_{\text{no}}(s_2, s_1) = \exp\left\{-\frac{s_1 - s_2}{\lambda_{\text{ph, min}}}\right\}. \quad (\text{A4})$$

The first term in square brackets corresponds to the probability that no interaction was sampled in the interval $(0, s)$. The second term is the contribution which comes from an interaction point sampled at s_1 but rejected with the probability $1 - \lambda_{\text{ph, min}}/\lambda_{\text{ph}}$.

The integration limits in (A3) ensure the ordering of the interaction points according to the simulation method, $0 < s_1 < s_2 < \dots < s$. Symmetrizing the integration limits yields

$$P_{\text{int}}(s)ds = \frac{ds}{\lambda_{\text{ph}}(E(s))} \exp\left\{-\frac{s}{\lambda_{\text{ph, min}}}\right\} \times \sum_{n=0}^{\infty} \frac{1}{n!} \left[\int_0^s ds' \left(\frac{1}{\lambda_{\text{ph, min}}} - \frac{1}{\lambda_{\text{ph}}(E(s'))} \right) \right]^n = \exp\left\{-\int_0^s \frac{ds'}{\lambda_{\text{ph}}(E(s'))}\right\} \frac{ds}{\lambda_{\text{ph}}(E(s))}, \quad (\text{A5})$$

which is identical to (A2) and shows that the described simulation method reproduces the correct, energy-dependent interaction length.

APPENDIX B: IMPLEMENTATION OF THE MAGNETIC FIELD

A turbulent magnetic field which is frozen into a fluid with fully developed hydrodynamic turbulence would follow a Kolmogorov spectrum, which is defined by

$$I(k) = I_0(k/k_0)^{-5/3} \quad (\text{B1})$$

where k is the wavenumber [31]. $I(k)$ is the energy density per unit wave number, k_0 the smallest wavenumber of the turbulence, the inverse k_0^{-1} is sometimes called the ‘‘cell size’’ of the turbulence. Hence we have for the total energy density [32]

$$U_{\text{tot}} = \frac{B_{\text{rms}}^2}{8\pi} = \int dk I(k). \quad (\text{B2})$$

In the propagation program we consider 3 discrete wave numbers. Thus we have to rewrite this integral in terms of a discrete spectrum in k , starting with k_0 and continuing with $k_i = 2k_{i-1}$, $i = 1, 2$. These are equally spaced apart in $\log_2 k$, with $\Delta(\log_2 k) = 1$. Hence the energy density we should ascribe to each of the three wavenumbers is approximately

$$U_i \approx \frac{I(k) dk}{d(\log_2 k)} \Big|_{k_i} \Delta(\log_2 k) = I_0 k_0 \ln 2 \left(\frac{k_i}{k_0}\right)^{-2/3}. \quad (\text{B3})$$

The total energy density is then a simple sum,

$$\frac{B^2}{8\pi} = U_0 + U_1 + U_2. \quad (\text{B4})$$

We normalize the field to a total energy density corresponding to $\langle |B| \rangle = 1 \text{ nG}$, i.e. $U_{\text{tot}} \approx 4 \times 10^{-20} \text{ erg cm}^{-3}$.

The technical implementation of the magnetic field into our propagation code is as follows. We divide the propagation volume into cubes of 1 Mpc side length, and attach to each of them a homogeneous field \mathbf{B}_0 with magnitude B_0 and random direction. Each of these cubes is divided into 8 cubes of 0.5 Mpc side length, to which a field \mathbf{B}_1 of magnitude B_1 and random direction is vectorially added to the field \mathbf{B}_0 . The procedure is repeated once more, so that our field is eventually realized on elementary cubes of 0.25 Mpc side length, each of which carries a magnetic field $\mathbf{B}_0 + \mathbf{B}_1 + \mathbf{B}_2$. We check that $\text{div} \mathbf{B} \simeq 0$ by approximating the surface integral with the sum of the outward normal component of \mathbf{B} over the surface of the $8 \times 8 \times 128 \text{ Mpc}^3$ volume V . The volume averaged value of $\text{div}(\mathbf{B})$ is calculated as

$$\langle \nabla \cdot \mathbf{B} \rangle = \frac{1}{V} \sum \mathbf{B}_{\perp} ds. \quad (\text{B5})$$

The r.m.s. value of $\langle \nabla \cdot \mathbf{B} \rangle$ for 10,000 field realizations is $\langle \nabla \cdot \mathbf{B} \rangle_{\text{rms}} = 3.7 \times 10^{-6} \text{ nG/kpc}$.

We also calculate the effective correlation length ℓ_{corr} by equating

$$\langle \mathbf{B}(\mathbf{x}) \cdot \mathbf{B}(\mathbf{x} + \xi) \rangle = B^2(\mathbf{x}) \exp\left(-\frac{|\xi|}{\ell_{\text{corr}}}\right). \quad (\text{B6})$$

The best fit value of ℓ_{corr} is 390 kpc.

